REPORT DOCUMENTATION PAGE

Form Approved OMB NO. 0704-0188

1. REPORT DATE (DD-MM-YYYY)	2. REPORT TYPE	3. DATES COVERED (From - To)
	New Reprint	-

4. TITLE AND SUBTITLE
Impact Point Prediction for Thrusting Projectiles inthe Presence of Wind

5a. CONTRACT NUMBER
W911NF-10-1-0369

5b. GRANT NUMBER

5c. PROGRAM ELEMENT NUMBER
611102

6. AUTHORS
Ting Yuan, Yaakov Bar-Shalom, Peter Willett, University of Connecticut, David Hardiman, AMRDEC

5d. PROJECT NUMBER

5e. TASK NUMBER

5f. WORK UNIT NUMBER

7. PERFORMING ORGANIZATION NAMES AND ADDRESSES
University of Connecticut - Storrs
438 Whitney Road Ext., Unit 1133

Storrs, CT 06269 -1133

8. PERFORMING ORGANIZATION REPORT NUMBER

9. SPONSORING/MONITORING AGENCY NAME(S) AND ADDRESS(ES)
U.S. Army Research Office
P.O. Box 12211
Research Triangle Park, NC 27709-2211

10. SPONSOR/MONITOR'S ACRONYM(S)
ARO

11. SPONSOR/MONITOR'S REPORT NUMBER(S)
57823-CS.44

12. DISTRIBUTION AVAILIBILITY STATEMENT
Approved for public release; distribution is unlimited.

13. SUPPLEMENTARY NOTES
The views, opinions and/or findings contained in this report are those of the author(s) and should not contrued as an official Department of the Army position, policy or decision, unless so designated by other documentation.

14. ABSTRACT
Wind can and often does significantly affect impact-point prediction (IPP) performance for thrusting/ ballistic endoatmospheric
projectiles. Wind exacerbates the estimation ambiguity between drag and thrust in the dynamic model and induces additional
uncertainty in the IPP procedure. A tracker accounting for the wind effect is presented and simulation study shows

15. SUBJECT TERMS
multiple interacting multiple model estimators, extended Kalman filter, impact point prediction, wind effect

16. SECURITY CLASSIFICATION OF:			17. LIMITATION OF ABSTRACT	15. NUMBER OF PAGES	19a. NAME OF RESPONSIBLE PERSON
a. REPORT	b. ABSTRACT	c. THIS PAGE			Yaakov Bar-Shalom
UU	UU	UU	UU		19b. TELEPHONE NUMBER 860-486-4823

Report Title

Impact Point Prediction for Thrusting Projectiles inthe Presence of Wind

ABSTRACT

Wind can and often does significantly affect impact-point prediction (IPP) performance for thrusting/ ballistic endoatmospheric
projectiles. Wind exacerbates the estimation ambiguity between drag and thrust in the dynamic model and induces additional
uncertainty in the IPP procedure. A tracker accounting for the wind effect is presented and simulation study shows that it can be
fully compensated if the wind information is available. An N-point adaptive initialization based on a goodness-of-fit test and a
statistical significance test is introduced. Based on the multiple interacting multiple model (MIMM) approach developed recently,
the IPP performance is investigated with respect to the total observation time and the sensor accuracy in various wind scenarios.
In each Monte Carlo (MC) run of the simulation study, under the same sensor accuracy and the same observation time, the
same set of random numbers has been used (but different in different MC runs) for the same caliber projectile in various wind
scenarios to examine how much the wind affects the IPP performance with/without the exact knowledge of the wind information.
The final conclusion is that with the wind effect accounted for, the IPP performance in the presence of wind is practically the
same as in its absence.

REPORT DOCUMENTATION PAGE (SF298)
(Continuation Sheet)

Continuation for Block 13

ARO Report Number 57823.44-CS
Impact Point Prediction for Thrusting Projectiles ...

Block 13: Supplementary Note

Approved for public release; distribution is unlimited.

Impact Point Prediction for Thrusting Projectiles in the Presence of Wind

Ting Yuan, Yaakov Bar-Shalom and Peter Willett

University of Connecticut

{tiy, ybs, willett}@engr.uconn.edu

David Hardiman

AMRDEC

david.hardiman@us.army.mil

November 30, 2012

Abstract

Wind can and often does significantly affect impact-point prediction (IPP) performance for thrusting/ ballistic endoatmospheric projectiles. Wind exacerbates the estimation ambiguity between drag and thrust in the dynamic model and induces additional uncertainty in the IPP procedure. A tracker accounting for the wind effect is presented and simulation study shows that it can be fully compensated if the wind information is available. An N-point adaptive initialization based on a goodness-of-fit test and a statistical significance test is introduced. Based on the multiple interacting multiple model (MIMM) approach developed recently, the IPP performance is investigated with respect to the total observation time and the sensor accuracy in various wind scenarios.

In each Monte Carlo (MC) run of the simulation study, under the same sensor accuracy and the same observation time, the same set of random numbers has been used (but different in different MC runs) for the same caliber projectile in various wind scenarios to examine how much the wind affects the IPP performance with/without the exact knowledge of the wind information. The final conclusion is that with the wind effect accounted for, the IPP performance in the presence of wind is practically the same as in its absence.

Index Terms

multiple interacting multiple model estimators, extended Kalman filter, impact point prediction, wind effect

---

Work supported by ARO W911NF-103-1-0369 and ONR N00014-10-1-0029.

I. Introduction

Impact point prediction (IPP) of a thrusting/ballistic projectile is significantly affected by wind. The wind effect, in addition to the short available observation time and the limited sensor accuracy, is an issue of high importance and concern.

The wind effect causes the moving projectile to turn into the "apparent" wind, i.e., wind causes the nose of the moving projectile to be pointed into the wind as observed from the projectile's (moving) frame of reference [6] [18]. A tail- or head-wind, if unaccounted for, would cause the IPP to give under- or over-prediction for the projectile's range (hence the term range wind effect); a cross wind would lead to left- or right-deviation. The vertical wind is ignored in this study, as it is typically not present. Consequently, the projectile's dynamic model is modified from [14] [15] to incorporate the wind effect. Based on the modified model, the sensitivity of the IPP performance with respect to the wind effect is studied.

The available observation time is a key factor that significantly affects the IPP performance and becomes even more critical in the presence of wind [6] [13]. For the IPP problem, using a state model with a drag coefficient and thrust estimated as separated components, there is an important observation-time tradeoff between accuracy and implementation of countermeasures. Before the prediction procedure starts, the collected measurements are used to initialize the estimator, attack the estimation ambiguity between the drag coefficient and the thrust components, and detect the probability of the correct mode converge close to unity [15]. The wind effect could impact each of these and evidently deteriorate the overall IPP performance.

Due to the nonlinear nature of the dynamics of the thrusting/ballistic projectiles, linearization and discretization of the nonlinear system is an approximation of reality. For a fixed sampling rate, the approximation quality is determined by the sensor accuracy. The observation uncertainty caused by the sensor errors (in range and azimuth/elevation angles) affects the estimation result, as well as the prediction procedure that follows, and hence the final IPP performance. Wind uncertainty exacerbates the observation uncertainty.

The present paper aims to offer an extensive analysis of the wind effect on the recently developed IPP system using a multiple interacting multiple model (MIMM) estimator (with different initial drag coefficient estimates and using unbiased mixing[1]) [15]. As an important practical issue, in many practical situations the wind information is not available. To examine how much effect this has on the IPP performance, three situations are considered, i.e., given perfect knowledge of the wind information (denoted concisely as "g.w.i." for later use), given no knowledge of the wind information ("n.w.i."), given the wind information with certain deterministic error ("e.w.i."). In order to provide a comprehensive insight, the IPP performance is investigated with respect to the total observation time and the sensor accuracy under various wind scenarios. It is worth

[1]The unbiased mixing of IMM estimator is the key for correct estimation of the extra components when the mode-matched filters of IMM estimator are of unequal dimensions, e.g., the thrust is the extra component in the present discussion.

noting that, for simplicity, we assume a constant wind during the estimation and prediction procedure (i.e., the whole trajectory period). Altitude/location-dependent wind can be easily dealt with in the same manner.

An N-point adaptive initialization based on a goodness-of-fit test and a statistical significance test is introduced. For each IMM estimator (associated with a selected drag coefficient) from the MIMM estimator, the initialization of the thrust component is of special importance when only a very short total observation time is available. A good initialization will alleviate the estimation ambiguity between the drag coefficient and the thrust. The N-point adaptive initialization particularly provides an early and reasonably accurate estimate between the drag coefficient and thrust (as well as the kinematic components) and leads to a quick identification of the correct mode of the IMM estimator.

The paper is organized in following manner. In Section II, the wind effect is presented and under a flat-Earth assumption (suitable for short range projectiles), the dynamic model in the *presence of wind* is modified from [15]. The corresponding discretized form of the modified dynamic model and the discrete-time measurement equations are also presented here. The MIMM estimator and the IPP procedure are described in Section III. The parameter setting, design of the MIMM estimator and the N-point adaptive initialization approach are presented in Section IV. Then in the presence of different wind (strength and direction) conditions, the IPP performance is investigated in various total observation time and sensor accuracy scenarios by simulation in Section V. Conclusions are presented in Section VI.

II. Dynamic Model and Measurement Model in the Presence of Wind

The wind effect, which worsens the estimation ambiguity between the drag coefficient and thrust [15] and thus presents an additional challenge to the IPP, must be carefully accounted for [3]. The sensitivity of the IPP performance to the drag coefficient estimate, which is significantly affected by the relative velocity of the projectile (even one with known shape) with respect to air, necessitates the quantification of the wind effect for the purpose of IPP.

The contribution of the wind comprises the range wind, cross wind and vertical wind effects. We ignore the last, since it is generally small; but the techniques we present could be augmented to account for it. A range (head/tail) wind will push back or forward the moving object and a cross wind causes the moving object deviate to the side. These wind components together are considered as the true wind velocity and are combined with the target velocity with respect to the ground to yield the so-called “apparent wind”. The moving target turns into the apparent wind, i.e., its nose is pointed into the wind (or “upwind”) while its tail pointing “downwind” [6] [18]. With the wind effect shown in Fig. 1, we have

$$\mathbf{v}_a = \mathbf{v}_w - \mathbf{v} \tag{1}$$

where $\mathbf{v}$ is the target velocity with respect to the ground, $\mathbf{v}_w$ is the wind velocity and $\mathbf{v}_a$ is the apparent wind velocity.

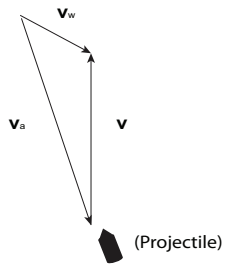

Fig. 1: The wind effect ($\mathbf{v}$ is the target's ground velocity, $\mathbf{v}_w$ is the wind velocity and $\mathbf{v}_a$ is the apparent wind velocity).

Thus, the drag and the thrust in the following dynamic model should be aligned with the direction of the projectile, which is aligned with the apparent wind. In the absence of information about how fast the projectiles align themselves with the apparent wind following launch, it is assumed that this happens instantaneously. During thrusting phase this is especially important, as due to wind thrust may thus not be aligned with the direction of travel.

For simplicity of analysis, we assume a constant wind during the estimation and prediction procedure (i.e., the whole trajectory period). The wind environment where the instantaneous projectile alignment hypothesis is reasonable and acceptable (e.g., altitude/location-dependent wind with slow variation or time-variant wind that is piecewise constant with respect to altitude) can be dealt with in the same manner.

In the presence/absence of wind, the trajectory of a thrusting projectile, from launch to impact, can be divided into two phases: thrusting and ballistic. It is a natural choice that we use an IMM estimator with a thrust mode (TM) and a ballistic mode (BM) to match these phases. The state vector for the corresponding TM is

$$\mathbf{x}(t) = [\, x(t) \;\; y(t) \;\; z(t) \;\; \dot{x}(t) \;\; \dot{y}(t) \;\; \dot{z}(t) \;\; \alpha(t) \;\; \tau(t) \,]' \tag{2}$$

where $\alpha(t)$ is the drag coefficient and $\tau(t)$ is the thrust. The state vector of the BM is the same as above but excludes the thrust component. The time arguments will be omitted where no ambiguity is caused.

Under flat-Earth assumption, the dynamic model *in the presence of wind* modified from [15] (the corresponding modifications are indicated by the sub-script "a", which implies the use of "apparent" wind information) can be written as follows

$$\begin{bmatrix} \ddot{x} \\ \\ \ddot{y} \\ \\ \ddot{z} \end{bmatrix} = \frac{\tau}{V_a} \begin{bmatrix} \dot{x}_a \\ \\ \dot{y}_a \\ \\ \dot{z}_a \end{bmatrix} + \alpha\, \alpha_m\, D_a \begin{bmatrix} \dot{x}_a \\ \\ \dot{y}_a \\ \\ \dot{z}_a \end{bmatrix} + \mathbf{g} + \tilde{\nu}_1 \tag{3}$$

and

$$\dot{\alpha} = \tilde{\nu}_2 \tag{4}$$

$$\dot{\tau} = \tilde{\nu}_3 \tag{5}$$

where

- The target velocities with respect to air are $\dot{x}_a \triangleq \dot{x} - \dot{x}_w$, $\dot{y}_a \triangleq \dot{y} - \dot{y}_w$ and $\dot{z}_a \triangleq \dot{z} - \dot{z}_w$.
- The first term on the right side of (3) is the specific thrust in the x, y, and z directions with accounting for the wind effect. For the ballistic phase, the thrust is zero.
- The second term is the drag part, which is related to the altitude and target velocity with respect to air.
- V_a is the magnitude of the velocity $[\ \dot{x}_a \quad \dot{y}_a \quad \dot{z}_a\ ]'$, i.e., the speed (in m/ s).
- α is the drag coefficient (in m^2/kg) at subsonic speed and τ is the thrust (in $\mathrm{m/s}^2$). It is known that the drag coefficient varies significantly with the Mach number regime: subsonic, transonic and supersonic. This will be accounted for by the α_m as below.
- α_m is the (dimensionless) *Mach number-dependent drag coefficient multiplier*, which is approximated by a cubic spline curve shown in Fig. 2. The cubic spline curve is obtained by an interpolation process shown in detail in Appendix A.
- $D_a = -\frac{\rho(z)V_a}{2}$, where $\rho(z) = \rho_0 e^{-cz}$ is the air density (in $\mathrm{kg/m}^3$) at altitude z (in m) and c is the air density constant (in m^{-1}) [12].
- $\mathbf{g} \triangleq [\,0 \;\; 0 \;\; -g\,]'$ is the standard gravity vector. g is the standard acceleration due to gravity at sea level, assumed to be the same throughout the trajectory, with value 9.812 $\mathrm{m/s}^2$.
- $\tilde{\nu}_1$, $\tilde{\nu}_2$, and $\tilde{\nu}_3$ are assumed to be continuous-time zero-mean white Gaussian noises. The drag coefficient and thrust acceleration are thus modeled as Wiener processes with slow variation [1].

Combining the dynamic equations (3)–(5), we have the following compact form (accounting for the wind effect)

$$\dot{\mathbf{x}}(t) = f_w[\mathbf{x}(t),\ \mathbf{x}_w(t)] + \tilde{\nu}(t) \tag{6}$$

where

$$f_w[\mathbf{x}(t),\ \mathbf{x}_w(t)] = \begin{bmatrix} \dot{x}(t) \\ \dot{y}(t) \\ \dot{z}(t) \\ \tau(t)\dfrac{\dot{x}_a(t)}{V_a(t)} + \alpha(t)\alpha_m(t)D_a(t)\dot{x}_a(t) \\ \tau(t)\dfrac{\dot{y}_a(t)}{V_a(t)} + \alpha(t)\alpha_m(t)D_a(t)\dot{y}_a(t) \\ \tau(t)\dfrac{\dot{z}_a(t)}{V_a(t)} + \alpha(t)\alpha_m(t)D_a(t)\dot{z}_a(t) - g \\ 0 \\ 0 \end{bmatrix} \tag{7}$$

with the wind effect compensation vector

$$\mathbf{x}_w(t) = [\,0 \;\; 0 \;\; 0 \;\; \dot{x}_w(t) \;\; \dot{y}_w(t) \;\; \dot{z}_w(t) \;\; 0 \;\; 0\,]' \tag{8}$$

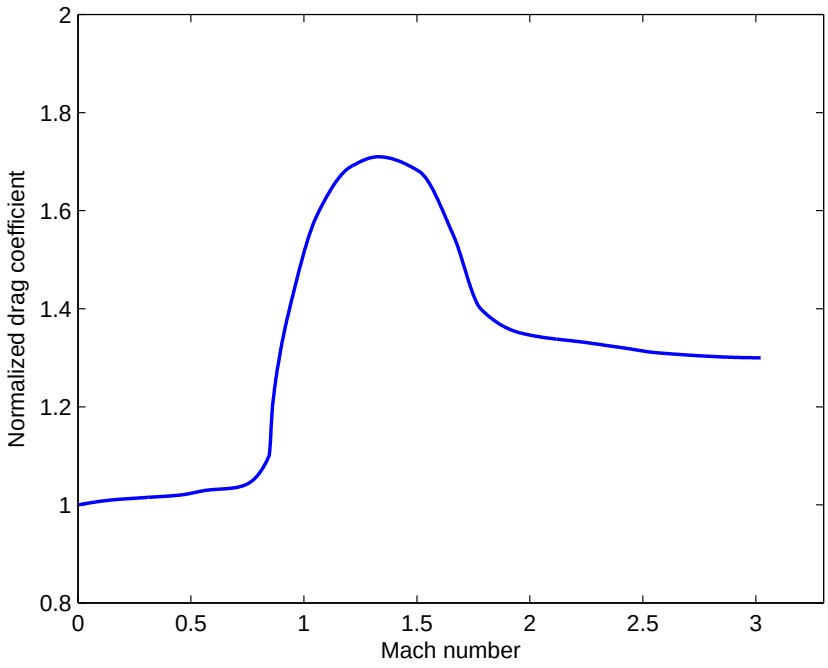

Fig. 2: The cubic spline approximation of the Mach number-dependent drag coefficient multiplier (for a "sharp nose" projectile [17]).

and the Wiener process vector

$$\tilde{\nu}(t) = [\,\tilde{\nu}_1(t)' \;\; \tilde{\nu}_2(t) \;\; \tilde{\nu}_3(t)\,]' \tag{9}$$

Note that $f_\alpha(\cdot)$ and $f_\tau(\cdot)$ are both equal to zero, as we assume the drag coefficient and thrust are Wiener processes.

The state vector equation is discretized by a second order Taylor expansion[2] [7]. Using the discrete time notation $\mathbf{x}(k) = \mathbf{x}(t)|_{t=kT}$ and $\mathbf{x}(k+1) = \mathbf{x}(t+T)|_{t=kT}$ (the same for $\mathbf{x}_w(t)$), we have the following discretized continuous-time expression [15]

$$\mathbf{x}(k+1) = \mathbf{x}(k) + f_w[\mathbf{x}(k), \mathbf{x}_w(k)]T + A_w(k) f_w[\mathbf{x}(k), \mathbf{x}_w(k)]\frac{T^2}{2} + \nu(k) \tag{10}$$

where $A_w(k)$ is the Jacobian of (7) evaluated at $\mathbf{x}(k)$ (with known wind information $\mathbf{x}_w(k)$) and $\nu(k)$ is the discretized continuous-time (white Gaussian) process noise for the sampling interval T. Based on the assumption that α is nearly constant and D_a is related to both z and V_a, the detailed form of A_w here is obtained by replacing in the Jacobian in [15] the target velocities (with respect to ground) with the corresponding target velocities with respect to air.

[2]It has been reported that for a short range ballistic projectile the first order Taylor expansion is sufficient. However, for the thrusting projectile with unknown drag coefficient and unknown thrust – as in the present study – the second order Taylor expansion is used to compensate for the nonlinearity made obscure by the unknowns. The methodology can be used for long range scenario, in which case a second order Taylor expansion is necessary to avoid bias [2].

The corresponding covariance matrix of the discretized process noise is

$$Q = \begin{bmatrix} \begin{bmatrix} \frac{T^3}{3} I_3 & \frac{T^2}{2} I_3 \\ \frac{T^2}{2} I_3 & T I_3 \end{bmatrix} q_v & \mathbf{0}_{6\times 1} & \mathbf{0}_{6\times 1} \\ \mathbf{0}_{1\times 6} & T q_\alpha & 0 \\ \mathbf{0}_{1\times 6} & 0 & T q_\tau \end{bmatrix} \tag{11}$$

where I_3 is the 3×3 identity matrix and the continuous time process noise "intensities" q_v, q_α and q_τ are the corresponding power spectral densities (PSD).

Assuming the sensor is located at $(\, x_s \;\; y_s \;\; z_s \,)$, the measurements in spherical coordinates are

$$r_m = r + w_r = \sqrt{(x - x_s)^2 + (y - y_s)^2 + (z - z_s)^2} + w_r \tag{12}$$

$$\theta_m = \theta + w_\theta = \tan^{-1}\left(\frac{y - y_s}{x - x_s}\right) + w_\theta \tag{13}$$

$$\epsilon_m = \epsilon + w_\epsilon = \tan^{-1}\left(\frac{z - z_s}{\sqrt{(x - x_s)^2 + (y - y_s)^2 + (z - z_s)^2}}\right) + w_\epsilon \tag{14}$$

where r, θ and ϵ are the independent true range, azimuth and elevation components, respectively. w_r, w_θ and w_ϵ denote the corresponding zero-mean white Gaussian measurement noises with standard deviations (SD) σ_r, σ_θ and σ_ϵ, respectively.

An unbiased measurement conversion from spherical to Cartesian coordinates was presented [2], so that the IPP problem can be described entirely in Cartesian coordinates:

$$\mathbf{z}(k) \triangleq H\mathbf{x}(k) + \mathbf{w}(k) \tag{15}$$

where $H = [\, I_3 \;\; \mathbf{0} \,]$, $\mathbf{w}(k)$ is the equivalent measurement noise vector in Cartesian coordinates obtained from the unbiased measurement conversion and $R(k)$ is the corresponding equivalent *state-dependent* covariance matrix.

III. Multiple-IMM Estimator for IPP

During the thrust mode (TM), the drag parameter (drag coefficient) and thrust parameter are separate state components as shown in (2). However, the drag force and thrust force are acting simultaneously (see equation (3)) and the IMM estimator has difficulty distinguishing between them if the initial uncertainty in the drag coefficient is large. A sudden decrease in the drag coefficient estimate may trigger an increase in the thrust estimate. In the presence of wind, the wind-induced motion makes correctly unsnarling these important components (drag coefficient and thrust) increasingly obdurate. The sensitivity of the estimation to the initial drag coefficient estimate necessitates the use of an MIMM estimator to overcome this "marginal observability" problem [1].

The procedure starts by establishing a set of the L IMM estimators, each with an appropriate set of modes (TM and BM in present case) to describe the system behavior. Each IMM estimator will be initialized with a different value of the drag

coefficient estimate with a suitable initial SD. The initial SD is taken equal to 25% of the initial estimate of the drag coefficient. The filtering parameter setting is discussed in Section IV.

In order to select the best initial drag coefficient estimate, we need to determine the most likely among L IMM estimators, during the observation period. The likelihood function of IMM estimator l for the time interval $[k_0,\, K]$ is

$$\Lambda_l^{k_0,K} = \prod_{k=k_0}^{K} \Lambda_l\,(k) \qquad\qquad l = 1, \ldots,\, L \tag{16}$$

where $\Lambda_l\,(k)$ is the likelihood function of lth IMM estimator, with r modes, at time k, given by [2]

$$\Lambda_l\,(k) \triangleq \quad \textstyle\sum_{i=1}^{r} \Lambda_l^i(k)\mu_l^i(k|k-1) \tag{17}$$

where $\Lambda_l^i(k)$ is the likelihood function of mode i of IMM estimator l at time k and $\mu_l^i(k|k-1)$ is the predicted mode probability for mode i of IMM estimator l. The mode likelihood is [1]

$$\begin{aligned}\Lambda_l^i(k) &= p\left[\mathbf{z}(k)|M_l^i(k), \hat{\mathbf{x}}_l^{0i}(k-1|k-1), P_l^{0i}(k-1|k-1)\right] \\ &= \mathcal{N}\left[\mathbf{z}(k); \hat{\mathbf{z}}_l^i(k|k-1), S_l^i(k)\right]\end{aligned} \tag{18}$$

where $\mathcal{N}\left[\,\cdot\,\right]$ is the Gaussian probability density function, $\hat{\mathbf{z}}_l^i$ is the predicted measurement and S_l^i is the innovation covariance in mode i of IMM estimator l. The predicted mode probability can be written as

$$\begin{aligned}\mu_l^i(k|k-1) &= \sum_{j=1}^{r} P\left\{M_l^i(k)|M_l^j(k-1), Z^{k-1}\right\} P\left\{M_l^j(k-1)|Z^{k-1}\right\} \\ &\triangleq \sum_{j=1}^{r} p_{ji}\mu_l^j(k-1)\end{aligned} \tag{19}$$

where $\mu_l^j(k-1)$ is the mode probability of mode j of IMM estimator l at time $k-1$ and p_{ji} is the transition probability from mode j to mode i over one time interval.

Using (18) and (19), one can rewrite (17) as

$$\Lambda_l(k) = \sum_{j=1}^{r} \left\{ \mathcal{N}\left[\mathbf{z}(k); \hat{\mathbf{z}}_l^i(k|k-1), S_l^i(k)\right] \sum_{j=1}^{r} p_{ji}\mu_l^j(k-1) \right\} \tag{20}$$

Then

$$l^* = \arg\max_l \Lambda_l^{k_0,K} = \arg\min_l \left[-\ln \Lambda_l^{k_0,K}\right] \tag{21}$$

selects the *best IMM estimator*. This yields the best initial estimate of the drag coefficient.

Based on the MIMM estimator, we can choose at the end of the observation period the most likely initial drag coefficient of the most probable mode from the best IMM estimator (21).[3] Then a numerical open-loop nonlinear predictor (we use the

[3]In practice, the thrusting period is relatively short and by the end of the observation period the BM should be the dominant one in the IMM. Otherwise, unless one were clairvoyantly to know the burnout time, one cannot make a meaningful IPP.

4th order Runge-Kutta (RK) method[4] [11], incorporating the wind effect if the wind information is available) is employed to predict the trajectory down to its impact point. At the same time, the corresponding covariance is also predicted to the impact point using a zero-gain (open loop) EKF covariance equation. Then the 99% chi-square probability region ellipse for the true impact point is [1]

$$[\, x_{ip} - \hat{x}_{pd} \;\; y_{ip} - \hat{y}_{pd} \,]\, P_{pd}^{-1} \begin{bmatrix} x_{ip} - \hat{x}_{pd} \\ \\ x_{ip} - \hat{y}_{pd} \end{bmatrix} = \chi_2^2\,(99\%) \tag{22}$$

where $(x_{ip} \;\; y_{ip})$ is the true impact point, $(\hat{x}_{pd} \;\; \hat{y}_{pd})$ is the predicted impact point, P_{pd} is the corresponding predicted covariance matrix, and $\chi_2^2\,(99\%)$ denotes the 99% point on the chi-square cumulative distribution function with two degrees of freedom [1]. This can be used as the "warning zone" in practical situations.

In practical situations the ellipse is centered at the predicted impact point and one can check whether the true impact point (if available) is within the 99% probability ellipse [15]. In Monte Carlo simulations, as in present study, we evaluate the (equivalent) converse: whether the predicted impact point falls into the ellipse centered at the true impact point [12].

The IPP procedure based on the MIMM estimator is shown in Fig. 3.

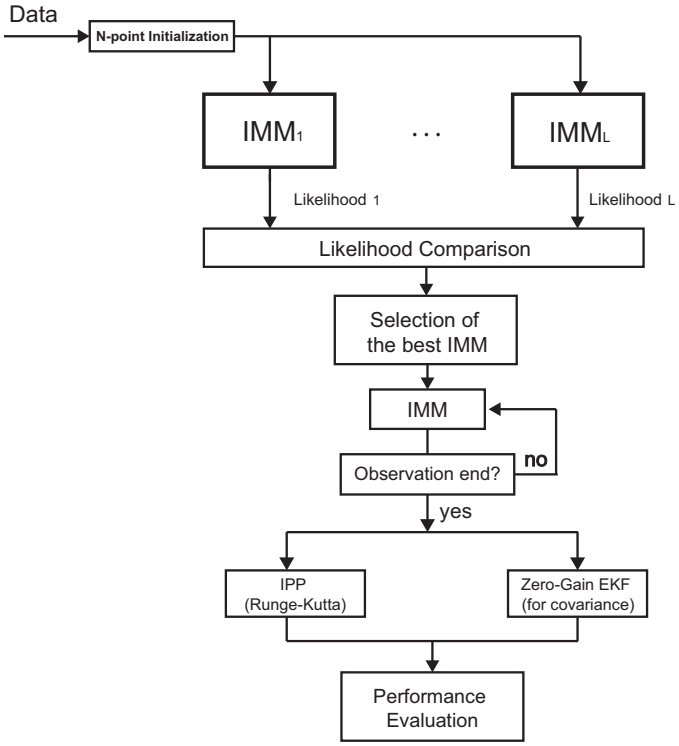

Fig. 3: The IPP procedure based on the MIMM estimator.

[4]Using the second-order open-loop EKF directly with a small iteration time interval (0.1 s) for the prediction shows IPP performance practically the same as the RK method.

IV. MIMM Design Parameter Selection

The MIMM estimator using unbiased mixing with different initial drag coefficient estimates is used [15]. The unbiased mixing is necessary because of the unequal dimension state vectors in the two modes (TM and BM).

A. MIMM for selection of the best initial drag coefficient estimates

The MIMM estimator is chosen to consist of $L = 4$ IMM estimators with initial drag coefficient estimates $\hat{\alpha}^i(0),\ i = 1, 2, 3, 4$ as 0.18, 0.13, 0.065 and 0.03 (m^2/kg), respectively.[5] The initial SD of each drag coefficient estimate is 25% of the corresponding initial estimate of the drag coefficient.

If the projectile library with the truth of the corresponding drag coefficient information is provided, the selection of the best initial estimate of the drag coefficient actually indicates the projectile identification [4] [12]. However, the wind effect could blur the identification.

B. N-point adaptive initialization

The initialization is crucial to the accuracy of the state estimates. Due to the sensitivity of the estimation on the drag coefficient, which is velocity (Mach number)-dependent and "marginally distinguishable" from the thrust estimate, an N-point adaptive initialization method is used here (the number N is discussed later). This method is based on the polynomial fitting of a set of noisy position measurements [1], with the polynomial order adaptively chosen based on the corresponding goodness-of-fit error. Particularly, it can give a good guideline for how to initialize the key thrust component.

The N-point fitting of a polynomial of order n is done as follows. The position measurements for the three Cartesian coordinates are

$$\begin{aligned} \mathbf{z}(k) &= H_{\mathbf{a}}(k)\mathbf{a} + w(k) \\ &\triangleq \begin{bmatrix} \mathbf{h}(k)' & \mathbf{0} & \mathbf{0} \\ \mathbf{0} & \mathbf{h}(k)' & \mathbf{0} \\ \mathbf{0} & \mathbf{0} & \mathbf{h}(k)' \end{bmatrix} \begin{bmatrix} \mathbf{a}_x \\ \mathbf{a}_y \\ \mathbf{a}_z \end{bmatrix} + w(k) \end{aligned} \tag{23}$$

where $k = 1, 2, \ldots, N$ and

$$\mathbf{h}(k) = \left[1 \ \ t_k \ \ \cdots \ \ \frac{(t_k)^n}{n!} \right]' \tag{24}$$

with t_k is the sampling time and the parameter vectors

$$\mathbf{a}_i = [\, a_{i0} \ \ a_{i1} \ \ \cdots \ \ a_{in} \,]' \qquad\qquad i = x,\ y,\ z \tag{25}$$

[5]This grid of values was chosen based on the tracking results in the absence of wind. It seems that the 60 mm projectile has a somewhat different drag coefficient in the presence of wind (it turns somewhat slowly into the wind, perhaps the result of a larger moment of inertia).

contain the coefficients of the polynomials (one for each coordinate).

For the time covered by N points, we get the estimate for the parameter vector $\mathbf{a}$ (of dimension $n_{\mathbf{a}} = 3(n+1)$) as

$$\hat{\mathbf{a}} = \left[H_{\mathbf{a}}^{N\prime} \left(R^N\right)^{-1} H_{\mathbf{a}}^N\right]^{-1} H_{\mathbf{a}}^{N\prime} \left(R^N\right)^{-1} \mathbf{z}^N \tag{26}$$

with the corresponding covariance matrix

$$P_{\mathbf{a}} = \left[H_{\mathbf{a}}^{N\prime} \left(R^N\right)^{-1} H_{\mathbf{a}}^N\right]^{-1} \tag{27}$$

where

$$\mathbf{z}^N = \begin{bmatrix} \mathbf{z}(1) \\ \vdots \\ \mathbf{z}(N) \end{bmatrix} \tag{28}$$

is the stacked vector of measurements (of dimension $3N \times 1$),

$$H_{\mathbf{a}}^N = \begin{bmatrix} H_{\mathbf{a}}(1) \\ \vdots \\ H_{\mathbf{a}}(N) \end{bmatrix} \tag{29}$$

is the stacked measurement matrix (of dimension $3N \times 3(n+1)$), and

$$R^N = \begin{bmatrix} R(1) & \cdots & \mathbf{0} \\ \vdots & \ddots & \vdots \\ \mathbf{0} & \cdots & R(N) \end{bmatrix} \tag{30}$$

is the block diagonal covariance matrix of measurement noise (of dimension $3N \times 3N$) for the fitting interval.

The goodness-of-fit error has the following chi-square distribution [1]

$$J_N \triangleq \left[\mathbf{z}^N - H_{\mathbf{a}}^N \hat{\mathbf{a}}\right]' \left(R^N\right)^{-1} \left[\mathbf{z}^N - H_{\mathbf{a}}^N \hat{\mathbf{a}}\right] \sim \chi^2_{3N-n_{\mathbf{a}}} \tag{31}$$

Using as acceptance region for (31) its 95% probability region (one-sided) and a component statistical significance test (a Gaussian test for the absolute value with 95% probability region, i.e., two-sided), we can adaptively choose the best order n^*, which avoids both "over-parameterizations" and "under-parameterizations" [1]. This is done by starting with $n = 1$ and increasing it until: (i) the test statistic (31) falls below the 95% probability threshold and (ii) the magnitude of at least one of the components (x, y and z) is statistically significant with the threshold $\mathcal{G}(97.5\%)$, which amounts to cutting the upper and lower tails of 2.5%.

The N-point adaptive initialization used $N = 12$ (about 1 s of data). As an illustrative example, Table I shows the results of the polynomial fitting of an observation sequence of the trajectory 60C7H7[6] with constant velocity (CV, $n = 1$), constant acceleration (CA, $n = 2$) and constant jerk (CJ, $n = 3$) models in one of the MC runs. For this particular case, the CA

[6]This stands for caliber 60 mm projectile in the presence of 7 m/s crosswind and 7 m/s headwind.

($n^* = 2$) model is chosen: the fitting error is $J_N^* = 44.0 < \chi^2_{3N-n_{\mathbf{a}}}(95\%) = 50.7$ and the z-component estimate magnitude is statistically significant: $2.3 > \mathcal{G}(97.5\%) = 1.96$. The test statistics that yielded the choice $n^* = 2$ are in boldface.

Remarks: Initialization of Thrust

In the present simulation study, the CV ($n = 1$) model and the CA ($n = 2$) model may be selected. For $n^* = 2$, the acceleration estimate is used (after subtracting the gravity acceleration and drag vector) to obtain the initial estimate of the thrust, $\hat{\tau}(0)$; for $n^* = 1$ (low thrust case), then $\hat{\tau}(0) = g$ with SD $g/4$.

TABLE I: Fitting of CV, CA and CJ models for trajectory 60C7H7 (with $\sigma_r = 10\,\text{m}$ and $\sigma_\theta = \sigma_\epsilon = 5\,\text{mrad}$)

Model	CV ($n=1$)			CA ($n=2$)			CJ ($n=3$)		
Component	x	y	z	x	y	z	x	y	z
$\hat{a}_{i0}$	0.9	-5.6	7.8	5.8	-17.2	-14.4	10.3	-20.9	-11.9
$\sqrt{P_{i0}}$	6.8	8.3	10.4	9.3	11.3	14.2	11.0	13.3	16.7
$\lvert\hat{a}_{i0}\rvert/\sqrt{P_{i0}}$	0.1	0.7	0.8	0.6	1.5	1.0	0.9	1.6	0.7
$\hat{a}_{i1}$	119.9	117.2	155.9	91.4	187.2	289.2	29.3	238.6	253.1
$\sqrt{P_{i1}}$	10.4	12.6	15.8	39.1	47.4	59.4	90.2	108.9	136.7
$\lvert\hat{a}_{i1}\rvert/\sqrt{P_{i1}}$	11.5	9.3	9.8	2.3	4.0	4.9	0.3	2.2	1.9
$\hat{a}_{i2}$				51.2	-127.4	-242.2	344.6	-369.4	-69.0
$\sqrt{P_{i2}}$				68.3	82.7	103.7	389.4	471.8	591.3
$\lvert\hat{a}_{i2}\rvert/\sqrt{P_{i2}}$				0.8	1.5	**2.3**	0.9	0.8	0.1
$\hat{a}_{i3}$							-531.9	437.7	-316.9
$\sqrt{P_{i3}}$							694.7	842.9	1055.6
$\lvert\hat{a}_{i3}\rvert/\sqrt{P_{i3}}$							0.8	0.5	0.3
J_N	*52.9*			**44.0**			43.3		
$\chi^2_{3N-n_{\mathbf{a}}}(95\%)$	52.0			50.7			49.5		

C. Selection of Process Noise Intensities

In the dynamic equations, we actually assume a nearly constant velocity model (continuous time white noise acceleration — CWNA [1]) for the kinematic components and a Wiener process with slow variation for the drag coefficient and thrust. In

order to satisfy this model's assumptions, we choose small process noise "intensities" (power spectral densities — PSD) q_v, q_α, and q_τ as follows.

The process noise induced root mean square (RMS) rate of change in velocity over an interval Δ is

$$d_v \triangleq \frac{\sqrt{q_v \Delta}}{\Delta} \ [(\mathrm{m/s})/\mathrm{s}] \tag{32}$$

For the drag coefficient the rate of change is

$$d_\alpha \triangleq \frac{\sqrt{q_\alpha \Delta}}{\Delta} \ [(\mathrm{m}^2/\mathrm{kg})/\mathrm{s}] \tag{33}$$

For the thrust the rate of change is

$$d_\tau \triangleq \frac{\sqrt{q_\tau \Delta}}{\Delta} \ [(\mathrm{m/s}^2)/\mathrm{s}] \tag{34}$$

Then we have the following estimator design procedure for selection of the process noise PSD based on the corresponding RMS rates of change

$$q_v = d_v^2 \Delta \ (\mathrm{m}^2/\mathrm{s}^3) \tag{35}$$

$$q_\alpha = d_\alpha^2 \Delta \ (\mathrm{m}^4/(\mathrm{kg}^2 \cdot \mathrm{s})) \tag{36}$$

$$q_\tau = d_\tau^2 \Delta \ (\mathrm{m}^2/\mathrm{s}^5) \tag{37}$$

The process noise intensities are chosen based on the process noise induced RMS change (in velocity/ drag coefficient/ thrust) over an interval of $\Delta = 1\,\mathrm{s}$ as shown in Table II. Note that d_v is chosen differently for the four initial drag coefficient estimates $\hat{\alpha}^i(0),\ i = 1, 2, 3, 4$.

TABLE II: The RMS change rate due to the process noise

Filter	d_v [(m/s)/s]				d_α [(m^2/kg)/s]	d_τ [(m/s^2)/s]
	$\hat{\alpha}^1(0)$	$\hat{\alpha}^2(0)$	$\hat{\alpha}^3(0)$	$\hat{\alpha}^4(0)$		
IMM (TM)	3.5	2.5	2	1	$0.12\hat{\alpha}^i(0)$/s	$0.25\,\hat{\tau}(0)$/s
IMM (BM)	1.6	1.4	1.2	0.9	$0.10\hat{\alpha}^i(0)$/s	N/A

D. IMM Mode Transition Probability Matrix

The Markov chain probability transition matrix for the two-mode IMM is

$$\pi = \begin{bmatrix} p_{11} & 1 - p_{11} \\ 1 - p_{22} & p_{22} \end{bmatrix} \tag{38}$$

where the elements of the matrix are obtained based on the mean sojourn time (MST) [1], s_1 and s_2, for the TM ($i = 1$) and the BM ($i = 2$) respectively

$$p_{ii} = 1 - \frac{T}{s_i} \qquad i = 1, 2 \tag{39}$$

and $T = 0.1\,\text{s}$ is the (fixed) sampling interval. Setting the MST as $s_1 = 2\,\text{s}$ and $s_2 = 50\,\text{s}$ for TM and BM respectively, we get the mode transition probability matrix

$$\pi = \begin{bmatrix} 0.950 & 0.050 \\ 0.002 & 0.998 \end{bmatrix} \tag{40}$$

with initial mode probability vector $[\,0.90 \;\; 0.10\,]$.

V. Simulation Results

Three categories of thrusting/ballistic projectiles of different calibers are considered: 60 mm, 81 mm and 120 mm. In all, 21 trajectories were generated using [16][7] with a flat-Earth model with quadrant elevation 45° (i.e., aimpoint is NE). The thrusting/ballistic projectiles are actually rocket-assisted with initial velocity around 250 m/s (which varies across different calibers). For each category, there are trajectories with no wind present, labeled as "W0"; with 5 m/s crosswind only, labeled as "C5"; with 10 m/s crosswind only, labeled as "C10"; with 5 m/s crosswind and 5 m/s headwind, labeled as "C5H5"; with 7 m/s crosswind and 7 m/s headwind, labeled as "C7H7"; with 5 m/s crosswind and 5 m/s tailwind, labeled as "C5T5"; with 7 m/s crosswind and 7 m/s tailwind, labeled as "C7T7". Note that the headwind blows against the motion of the projectiles while the tailwind blows in the travel direction of the projectiles [18]. Measurements were obtained with no missed detections and no false alarms.

The parameters of the trajectories of the different caliber projectiles considered, namely, the projectile range to impact (R^t), the impact time (T^t_{ip}), the sampling interval (T), the maximum ground speed (V^t_{max}), the ground speed at impact point (V^t_{ip}) and the apogee altitude (H^t_{apg}), are summarized in Table III. The launch point of each projectile was at the origin of coordinates. The sensor location was $(\,5000 \;\; 4000 \;\; 0\,)$ m.

As shown in Table IV, four different sensor accuracy settings are used and labeled as $Case\ 1$ (good sensor accuracy), $Case\ 2$ (poor angle accuracy), $Case\ 3$ (poor range accuracy) and $Case\ 4$ (the best sensor accuracy).

With 100 Monte Carlo (MC) runs for each sensor accuracy, we examine the IPP performance with given wind information (g.w.i.) and with no wind information provided (n.w.i.) for various *total observation time percentages of the whole trajectory* (denoted as "OT" for conciseness): 15%, 20%, 25%, 30%, 40% and 50%. In particular, under the same sensor accuracy and

[7]This is a high fidelity simulation for rocket-assisted projectiles, i.e., with initial "catapulted" velocity. The trajectories were generated based on models we cannot control and do not know.

TABLE III: The parameters of the trajectories of the different caliber projectiles considered

Caliber	R^t (m)	T_{ip}^t (s)	T (s)	V_{max}^t (m/s)	V_{ip}^t (m/s)	H_{apg}^t (m)
60 mm	3600 ± 100	30 ± 1	0.1	240 ± 3	155 ± 3	1085 ± 5
81 mm	5700 ± 150	37 ± 1	0.1	295 ± 3	200 ± 3	1680 ± 10
120 mm	7000 ± 250	41 ± 1	0.1	315 ± 5	230 ± 5	2055 ± 10

TABLE IV: Sensor accuracy settings

	σ_r	σ_θ	σ_ϵ
$Case\ 1$	10 m	5 mrad	5 mrad
$Case\ 2$	10 m	10 mrad	10 mrad
$Case\ 3$	25 m	5 mrad	5 mrad
$Case\ 4$	5 m	3 mrad	3 mrad

the same OT setting, in each MC run, the same random number set (but different in different MC runs, of course) has been used for different trajectories (W0/ C5/ C10/ C5H5/ C7H7/ C5T5/ C7T7) to examine how significantly the wind affects the IPP performance.

Three different situations concerning the knowledge of the wind information are considered: the "g.w.i." (perfect knowledge), the "n.w.i" (no knowledge) and the "e.w.i" (an inaccurate knowledge of 30% positive deterministic error, i.e., $\mathbf{v}_w + \mathbf{v}_b \triangleq \mathbf{v}_w + 0.3\mathbf{v}_w$, where $\mathbf{v}_b$ is a deterministic bias). Note that all the IPP results are *by default* obtained with "g.w.i." unless "n.w.i" or "e.w.i" is indicated. The indicating term "g.w.i." is omitted in Figures, Tables and discussions if there is no ambiguity.

A sample estimated trajectory, indicating the portions corresponding to the MIMM filtering and to the IPP, including the estimated burnout point (BoP) and the uncertainty ellipse centered at the true impact point, is presented in Fig. 4.

A. IPP RMS Error

The IPP root mean square (RMS) errors of the trajectories of caliber 60 mm, 81 mm and 120 mm (in various scenarios) are shown in Tables V, VI and VII, respectively. The g.w.i., n.w.i. and e.w.i. IPP RMS errors for various OTs and various sensor accuracies are evaluated and compared.

From Tables V–VII, it can be seen that, generally, as the wind becomes stronger, the difference between the g.w.i. IPP RMS error and the n.w.i. IPP RMS error will increase, especially for smaller OTs; as the OT increases, the influence of the wind on the IPP performance becomes smaller. As the sensor accuracy becomes worse, the IPP performance is gradually

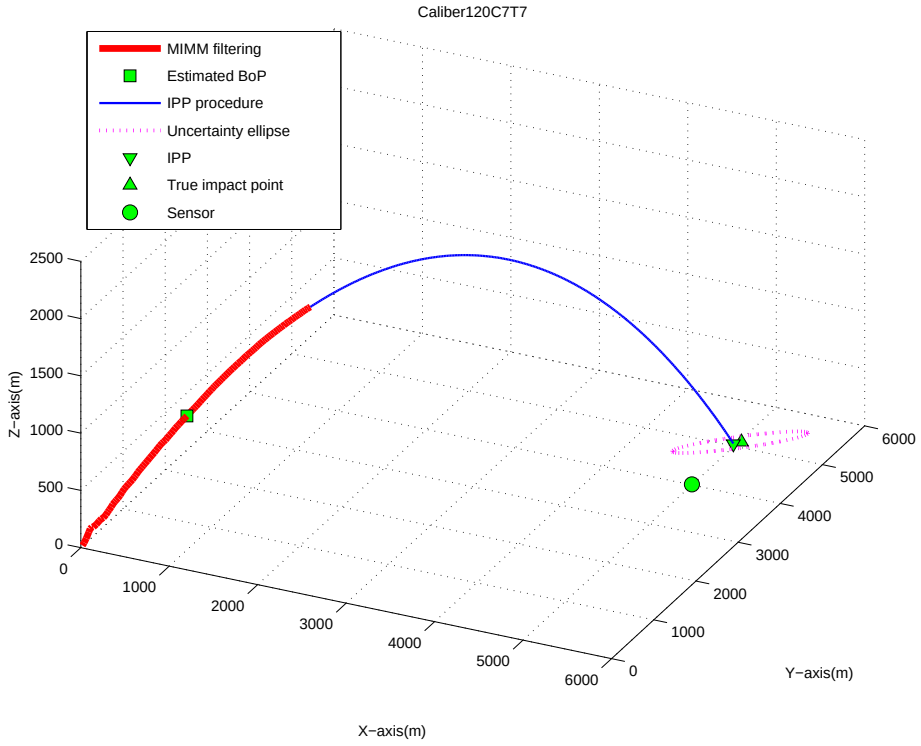

Fig. 4: A sample estimated trajectory with IPP uncertainty ellipse centered at true impact point.

degraded. Particularly, a sensor error that causes more uncertainty along the travel direction of the projectiles, compared with the sensor error that causes more uncertainty perpendicular to travel direction of the projectiles, has more influence on the IPP performance. In the presence of a weak wind (C5), the IPP RMS error (g.w.i.) is practically the same as the IPP RMS error (e.w.i.). The knowledge of the wind information with a small deterministic bias has small effect on the IPP performance.

We can get an IPP RMS error of more than $500\,\mathrm{m}$ for the $60\,\mathrm{mm}$ projectile (Table V: $Case$ 2, OT=15%), more than $650\,\mathrm{m}$ for the $81\,\mathrm{mm}$ (Table VI: $Case$ 3, OT=15%) and more than $750\,\mathrm{m}$ (even $900\,\mathrm{m}$) for the $120\,\mathrm{mm}$ (Table VII: $Case$ 2 and $Case$ 3, OT=15%). These are unacceptable errors.[8] A strong wind effect, combined with a poor sensor accuracy, can lead to an unacceptable IPP RMS error when only a very short total observation time is available. On the other hand, a good sensor accuracy in the presence of known wind (even with a small bias) always yields a good IPP performance.

In Tables V–VII, the columns with the wind information provided (g.w.i.) show that, given a sufficient observation time (say, OT= 25%– 50%) to correctly select the best IMM from the MIMM estimator (i.e., to overcome the "marginal observability" problem between the drag coefficient and thrust), the IPP RMS errors are practically the same as without wind.[9] This implies that the wind effect can be fully compensated if the wind information is correctly provided.

[8]In practical situations, a minimum acceptable IPP RMS error is expected to be within 10% of the projectile range. The IPP RMS errors larger than 10% of the projectile range are in *italic font* in Tables V–VII .

[9]This is highlighted by the IPP RMS errors shown in **bold font** in Tables V–VII .

TABLE V: IPP RMS errors (in m, 100 MC runs) for various OTs (shown in the first column) and various sensor accuracies, caliber 60 mm: *italic*, see footnote 8; **bold**, see footnote 9.

$Case\ 1$	60W0	60C5			60C10			60C5H5			60C7H7			60C5T5			60C7T7		
		g.w.i.	n.w.i.	e.w.i.	g.w.i.	n.w.i.	e.w.i.	g.w.i.	n.w.i.	e.w.i.	g.w.i.	n.w.i.	e.w.i.	g.w.i.	n.w.i.	e.w.i.	g.w.i.	n.w.i.	e.w.i.
15%	417.4	419.5	420.7	419.8	441.4	426.7	440.1	452.5	461	459.6	458.4	464.3	465.3	417.2	426.8	418.5	408.8	409.6	410.9
20%	152.1	150.8	154.7	151.3	150.4	169	157.3	145.6	129.5	138.7	142.1	136.4	130.2	158.2	182	180.1	157.7	191.5	195.2
25%	127	127.1	132.8	127.5	126.9	145.2	125.8	122.6	111.8	97.4	120.7	119	91.2	127.7	142.2	158.6	120.2	155.9	166.5
30%	106	105.6	111.2	107.1	108.5	124.1	108.5	96	85.2	75.6	94.3	94.9	70.9	108.8	121.4	133.9	101.5	129.7	137.9
40%	60.4	60.2	65.3	59.9	59.5	78.8	60.2	59.2	55.4	46.3	59.9	59.1	45.4	60.3	72.3	80	59	82.9	88.2
50%	**40**	**40**	44.8	40	**39.3**	56.1	40.8	**40.2**	39.5	30.2	**40.5**	42.3	29.7	**40.2**	50.4	53.7	**39.4**	55.9	59.9
$Case\ 2$	60W0	60C5			60C10			60C5H5			60C7H7			60C5T5			60C7T7		
		g.w.i.	n.w.i.	e.w.i.	g.w.i.	n.w.i.	e.w.i.	g.w.i.	n.w.i.	e.w.i.	g.w.i.	n.w.i.	e.w.i.	g.w.i.	n.w.i.	e.w.i.	g.w.i.	n.w.i.	e.w.i.
15%	*537.7*	*533.3*	*539.4*	*534.5*	*532.3*	*537.3*	*536.5*	*535.6*	*535.4*	*544.8*	*538.6*	*546.1*	*552.6*	*530*	*523.7*	*516.8*	*505.1*	*519.4*	*508.1*
20%	209.1	207.1	207.3	207.3	203.7	218.2	206	197.9	194.4	190	197.4	192.6	185.4	199.1	216.4	224.7	205	216.6	236.9
25%	149.2	149.1	154.8	150.4	148.9	167.1	154.6	147.1	135.9	122.1	143.9	133.2	115.5	155.8	173.7	187.1	155.2	184	205.4
30%	114.3	114	119.6	114.2	114.5	130.9	116.3	111.7	104.3	89.7	111.2	104.4	84.1	119.3	138.2	147.4	117.4	145.3	160
40%	65.6	65.4	70.9	65.5	65.3	83.2	67	67	63.3	52.3	66.1	65.3	47.8	66.4	80.4	85.3	65.9	88.2	95.3
50%	**47.6**	**47.4**	52.6	47.2	**47.3**	64.9	47.9	**47.1**	46.3	35.9	**45.4**	49.8	32.6	**49.5**	59.3	62.4	**49**	65.1	69.2
$Case\ 3$	60W0	60C5			60C10			60C5H5			60C7H7			60C5T5			60C7T7		
		g.w.i.	n.w.i.	e.w.i.	g.w.i.	n.w.i.	e.w.i.	g.w.i.	n.w.i.	e.w.i.	g.w.i.	n.w.i.	e.w.i.	g.w.i.	n.w.i.	e.w.i.	g.w.i.	n.w.i.	e.w.i.
15%	373.2	372.5	376.2	374.3	369.4	383.5	391.7	379.1	347.4	378.8	380	336.3	381.7	363.7	385.5	384	361.1	393.4	392.6
20%	337.7	339.8	337.4	349.8	353.6	345	372.7	368	369.3	398.5	370.1	384.1	404.3	332.9	350	336.8	342.3	353	346
25%	175.7	176.2	179.7	178.3	176.6	193.2	182.2	180.8	170.4	168.3	174.3	168.7	167.6	182.6	207.4	203.8	181.4	219.2	213.2
30%	140.2	138.6	141.2	138.8	140.2	162	149.4	143.4	138.3	135.3	142.6	138.8	136.3	155.4	169.3	170.9	144.2	181.8	162.3
40%	110.7	111.4	115.8	115.2	116.2	126	113.8	103.4	98.6	98.2	104.6	104.4	97.6	115	122.8	127	113.6	122.1	128.9
50%	**54.9**	**55.4**	59.2	57	**55.8**	69.5	58.7	**63**	65.6	61.1	**62.2**	68.6	60.8	**57.5**	63.7	62.6	**58.4**	68	66.3
$Case\ 4$	60W0	60C5			60C10			60C5H5			60C7H7			60C5T5			60C7T7		
		g.w.i.	n.w.i.	e.w.i.	g.w.i.	n.w.i.	e.w.i.	g.w.i.	n.w.i.	e.w.i.	g.w.i.	n.w.i.	e.w.i.	g.w.i.	n.w.i.	e.w.i.	g.w.i.	n.w.i.	e.w.i.
15%	242.9	242.8	248.2	245	239.8	262	260.3	239	233.6	244.7	241.7	235.1	256.7	249.5	259.6	263.6	247.6	272.5	265.4
20%	137.4	139.4	143.1	140.8	138.3	159.6	147.7	137	132.8	116.5	136.6	133.3	116.8	140.6	166.4	178.3	140.6	173.6	189.3
25%	114.3	114	122.3	112	109.9	137.6	118.3	113.2	115.6	89.3	112.4	118.1	82.1	107.6	132.8	148.6	109.1	141.1	161.8
30%	88.7	89	96.7	90.1	88.3	112.2	96.2	89.4	88.1	71.1	89.1	91.9	70.2	86.5	102.7	118.3	84.5	109.9	127.4
40%	53.7	53.7	61.4	53.7	52.6	75	57.2	53.3	52.1	39.2	53	56.2	38.9	51.5	66.3	73.5	52.3	73.2	83
50%	**38.8**	**38.9**	42.5	38.6	**38.2**	52	40.7	**36.7**	36.4	26.6	**36.6**	39	25.6	**37.8**	46.8	52.2	**37.8**	52	58.3

From Tables V–VII, an interesting observation is that for the situations with headwind and very short observation time, e.g., C5H5 and C7H7 with small OTs (e.g., OT=15% or 20%), the g.w.i. IPP RMS performance is counter-intuitively worse than the n.w.i. IPP RMS performance. This is because of the imperfect selection of which is the best IMM in the MIMM estimator when it is based on a very short observation time. More clearly, as shown in Fig. 5 (the trajectory 60C7H7 in $Case$

TABLE VI: IPP RMS errors (in m, 100 MC runs) for various OTs (shown in the first column) and various sensor accuracies, caliber 81 mm: *italic*, see footnote 8; **bold**, see footnote 9.

$Case\ 1$	81W0	81C5			81C10			81C5H5			81C7H7			81C5T5			81C7T7		
		g.w.i.	n.w.i.	e.w.i.	g.w.i.	n.w.i.	e.w.i.	g.w.i.	n.w.i.	e.w.i.	g.w.i.	n.w.i.	e.w.i.	g.w.i.	n.w.i.	e.w.i.	g.w.i.	n.w.i.	e.w.i.
15%	420.8	420.1	424.1	422.2	420	438.7	427.4	401.8	423.3	428.6	389.3	436.2	399.1	421.1	382.8	414.3	420.3	384.9	415
20%	432.4	428.4	438.6	429	428	445.9	430.9	423.4	401.8	384.1	418.6	393.2	361.2	428.7	456.5	481.9	430.1	475.5	497.6
25%	288.9	294.4	294.5	292.3	292.7	300.6	296.3	292.3	260.8	254.7	291.1	257.4	240.3	282.7	323.6	333	285.2	343.8	352.6
30%	188	186	193.3	186.8	185	204.1	190	190.2	181.2	158	196.6	183.3	148.5	189.3	206	230.1	191.5	221.3	246
40%	101.1	100.5	104.8	101	100.8	118.5	103.4	99.4	96.7	80.4	99	96.8	72.7	99.3	114.2	127.1	101	122.4	141.6
50%	**48.7**	**48.8**	51.8	48.6	**49.7**	62.2	51.6	**48.5**	47.9	40.1	**47.7**	49.7	36.8	**48.5**	58.6	63.7	**49.5**	64.5	71.9
$Case\ 2$	81W0	81C5			81C10			81C5H5			81C7H7			81C5T5			81C7T7		
		g.w.i.	n.w.i.	e.w.i.	g.w.i.	n.w.i.	e.w.i.	g.w.i.	n.w.i.	e.w.i.	g.w.i.	n.w.i.	e.w.i.	g.w.i.	n.w.i.	e.w.i.	g.w.i.	n.w.i.	e.w.i.
15%	497.5	492	492.2	491.4	482.9	501.6	484.2	490.5	520.3	500.4	511.8	504.4	528.4	491.9	526.6	494.1	486.7	534.8	500.7
20%	450.5	449.6	451.7	448.9	448.9	459.7	448.8	451.7	416.9	398.2	441.6	401.2	383	444.3	467.6	486.7	449.9	495.5	510.2
25%	315.7	313.6	320	317	313.1	328.4	318.4	318.8	295.6	283	317.8	285.9	269.3	317.1	354.3	359.6	320	376.9	377.2
30%	209.5	209	217.1	209.8	208.4	230.2	211.6	209.3	204.6	175.3	217.2	214.8	174.7	212.5	239.6	251.8	213.7	257.8	267.3
40%	133.8	135.2	140	135.4	134.9	151.3	137.1	135.3	130	111.5	134.9	130.9	103.3	131	150.9	157.7	129.3	159.9	166.4
50%	**68.9**	**69.1**	73	68.6	**72.7**	87.5	73.6	**72.1**	69.7	57.9	**71.8**	71.7	53.1	**69.1**	80.1	86.1	**69.6**	87.7	94.7
$Case\ 3$	81W0	81C5			81C10			81C5H5			81C7H7			81C5T5			81C7T7		
		g.w.i.	n.w.i.	e.w.i.	g.w.i.	n.w.i.	e.w.i.	g.w.i.	n.w.i.	e.w.i.	g.w.i.	n.w.i.	e.w.i.	g.w.i.	n.w.i.	e.w.i.	g.w.i.	n.w.i.	e.w.i.
15%	*665.2*	*665*	*667.1*	*665.9*	*652.6*	*675.7*	*659.2*	*664.8*	*661.7*	*643.9*	*690.8*	*703.7*	*668.2*	*646.5*	*673.5*	*667.4*	*651.7*	*687.6*	*667.4*
20%	479.9	479.6	480.9	479.7	485	490.7	490.9	478.3	473.4	456	472.8	471.7	445.3	476.8	473.2	504.8	476.6	501.9	516.7
25%	344.9	345.1	349.3	346.4	348.2	362.3	352.3	351.4	327.9	331	348.3	320.9	325.5	347.4	375.1	365.2	346.9	372.1	376
30%	213.5	213.7	216.9	212	217.5	229.5	218.2	212.7	201.5	190.4	223.4	203.3	208.9	217.9	240.9	238.4	219.1	248.8	252.2
40%	131.2	127.2	136.6	126.9	126.9	144.4	131.7	131.4	130.7	124.4	128.4	134.1	129.7	131.6	145.5	139.4	129.9	143	145.2
50%	**66.7**	**67**	70.4	67	**63.9**	74.8	67.1	**62.5**	63	60.4	**64**	65.3	60	**66.8**	71.1	76.4	**67.7**	77.8	83
$Case\ 4$	81W0	81C5			81C10			81C5H5			81C7H7			81C5T5			81C7T7		
		g.w.i.	n.w.i.	e.w.i.	g.w.i.	n.w.i.	e.w.i.	g.w.i.	n.w.i.	e.w.i.	g.w.i.	n.w.i.	e.w.i.	g.w.i.	n.w.i.	e.w.i.	g.w.i.	n.w.i.	e.w.i.
15%	465.4	465	468.2	465.2	464.9	479.5	467.3	464.9	444.7	395.7	445.1	451.4	375.8	464.7	469.2	520.1	463	483	549.7
20%	322.4	322	332.9	322.3	321.5	342.7	323.6	324.1	294.5	268	323.2	286.4	256.3	317.9	362.1	368.7	301.1	367.5	375.8
25%	199.8	202.1	208.2	203.1	202	223.4	206.9	200.4	176.8	165	198.5	174.7	154	201.8	235	242.5	205.2	252.5	261.4
30%	123.9	122.4	129.1	123.2	121.3	145.6	130.2	121.1	120.6	95.8	124.3	138	94.3	122.6	140.2	166.6	121.2	151.4	184.8
40%	67.7	67.7	73.5	68.8	67.7	85.2	72.6	67.4	65.6	52.7	67.5	68.2	50.9	67.8	80.8	91.8	65.7	87.7	101.6
50%	**33.5**	**33.2**	37.3	34.7	**36.2**	48.6	40.8	**36.2**	35.5	28.1	**35.9**	37.6	28.3	**33.8**	42.7	49.2	**34**	48.2	58.1

3 and OT=15%), because of this imperfect decision of the best IMM, each MC IPP "cloud of points" (for g.w.i. and n.w.i.) is approximately separated into 3 different clusters, designated as the "cluster A", "cluster B" and "cluster C". It can be seen, compared with the g.w.i. clusters, that the n.w.i. clusters have a clear drift caused by the wind effect. By coincidence, this drift happens to drive "cluster A (n.w.i.)" that contains the most points of the MC IPP closer to the true impact point. This

TABLE VII: IPP RMS errors (in m, 100 MC runs) for various OTs (shown in the first column) and various sensor accuracies, caliber 120 mm: *italic*, see footnote 8; **bold**, see footnote 9.

$Case\ 1$	120W0	120C5			120C10			120C5H5			120C7H7			120C5T5			120C7T7		
		g.w.i.	n.w.i.	e.w.i.	g.w.i.	n.w.i.	e.w.i.	g.w.i.	n.w.i.	e.w.i.	g.w.i.	n.w.i.	e.w.i.	g.w.i.	n.w.i.	e.w.i.	g.w.i.	n.w.i.	e.w.i.
15%	718.2	718.2	720	718.1	717.8	714.7	718.8	749.5	653.1	714.2	*753.2*	652.5	698.9	684.6	*760.6*	723.1	681.3	779.5	745.6
20%	547.4	546.7	548.5	547.4	539.6	555.6	544.5	576.7	562.3	534.9	572.4	575.6	477.1	581.2	571.5	651.9	591.7	585.5	699.5
25%	488.9	492.6	492	492.9	491.9	497.4	497.9	488.5	474	416.3	484.2	465.9	391.2	502.9	521.7	552.4	494.8	513.7	578
30%	308.6	308.4	315.5	308.4	307.8	330.4	308.9	306.4	292.7	261.8	302	284.7	243.5	313	334	354.3	316	337.8	368.4
40%	117.5	115	122.6	115.8	114.8	132.6	117	114.6	116.6	100.4	115.4	118	94.9	121.5	130.1	142.2	118.2	128.7	150.7
50%	**55.1**	**54.9**	58.8	56.6	**56**	67.2	59.8	**52.4**	55.4	52.9	**51.4**	57.5	54	**56**	60.6	62.6	**56.7**	64.1	66.8
$Case\ 2$	120W0	120C5			120C10			120C5H5			120C7H7			120C5T5			120C7T7		
		g.w.i.	n.w.i.	e.w.i.	g.w.i.	n.w.i.	e.w.i.	g.w.i.	n.w.i.	e.w.i.	g.w.i.	n.w.i.	e.w.i.	g.w.i.	n.w.i.	e.w.i.	g.w.i.	n.w.i.	e.w.i.
15%	*779.2*	*776.3*	*790.9*	*775.8*	*782.2*	*789*	*777.1*	*769.3*	748.9	*766.6*	*786*	725.8	*756.8*	*761.2*	*797.5*	*773.3*	744.9	*788.3*	*795.7*
20%	613.3	613.3	618	612.3	616	622.6	614.8	597.5	593.1	535.7	607.2	571.8	509.9	624.1	631.1	693.5	621.4	653.9	725
25%	489.8	494.1	492.5	493.5	493.6	497.9	492.9	493.2	480.9	450	497.5	473.7	419.3	493.9	500.7	557.1	475.7	486.2	551.6
30%	346.7	348.2	349.8	347.7	347.9	354.3	345.2	362	346.4	317.5	359.7	344.5	299.6	345.9	368.2	387.8	342	381.2	414.3
40%	144.5	142.9	148.8	143.5	142.3	158.3	144.4	144.9	148.7	126.7	144.9	149.1	119.6	152.3	159.1	179.4	156.4	174.1	197.2
50%	**63**	**61.5**	66.7	62	**61.1**	75.7	63.4	**61.6**	63.4	53.7	**59.8**	64.8	50.4	**64.7**	69.1	79.6	**63.1**	73.8	84.9
$Case\ 3$	120W0	120C5			120C10			120C5H5			120C7H7			120C5T5			120C7T7		
		g.w.i.	n.w.i.	e.w.i.	g.w.i.	n.w.i.	e.w.i.	g.w.i.	n.w.i.	e.w.i.	g.w.i.	n.w.i.	e.w.i.	g.w.i.	n.w.i.	e.w.i.	g.w.i.	n.w.i.	e.w.i.
15%	*887.6*	*879.9*	*885.9*	*879.6*	*879.2*	*889*	*879.3*	*874.7*	*859.6*	*833.7*	*870.8*	*867.2*	*817.1*	*883.2*	*894.5*	*918.5*	*878.7*	*901.2*	*936.4*
20%	650.1	651.2	654.4	652.9	648.6	659.1	643.8	634.1	611.4	612.4	642.2	608.4	607.2	639.8	686.1	673.8	642.7	697.9	685.1
25%	446.3	446.4	443.7	433.6	431.7	445	431.3	449.1	397.7	433.1	437.6	395.9	425.4	426.6	465.4	450.9	398.9	422.2	452.6
30%	279.3	271.4	281.5	272.5	270.1	302.4	275.9	284.4	277.7	273.1	285.7	275.8	265.9	272.5	284.1	294.4	272.4	286.6	314.3
40%	130.5	130.8	135.6	131	127.1	146.5	133	136.7	135.4	132.3	134.3	138.6	131.7	129.1	139.5	132.4	133.3	151.4	144
50%	**64.9**	**65.1**	68.1	67.7	**64.4**	75	71	**64.3**	67.3	65.5	**64.1**	70.2	66.6	**66.7**	70.3	68.1	**62.6**	68.1	71.5
$Case\ 4$	120W0	120C5			120C10			120C5H5			120C7H7			120C5T5			120C7T7		
		g.w.i.	n.w.i.	e.w.i.	g.w.i.	n.w.i.	e.w.i.	g.w.i.	n.w.i.	e.w.i.	g.w.i.	n.w.i.	e.w.i.	g.w.i.	n.w.i.	e.w.i.	g.w.i.	n.w.i.	e.w.i.
15%	462.7	462.4	462.2	477.3	476.6	468.3	482.2	480.2	445.6	426.4	464.8	456.8	453.1	464.1	534.3	533.8	474.7	528.1	590.9
20%	433.9	433.3	433.8	434.1	430.2	448.5	434.6	413.3	420.6	350.8	413.8	445.6	306.8	444	430.8	506	456	437.5	543.7
25%	337.4	336.6	340.7	336.9	335.5	353.1	339.8	323.9	318.7	276	321.8	321.2	260	350.1	360.3	394.8	329.5	368.2	398.2
30%	198.1	198	206.4	196.7	196	213.1	200.7	177.9	170.4	151.8	178.9	172.2	143.1	207.9	221.4	246.6	211	235.1	268.4
40%	62.2	62	65.1	62.9	61.4	76	67.6	61.8	65.8	59.7	59.9	69.2	64.2	64.5	68.9	80.2	67.7	77.8	93
50%	**29.5**	**29.4**	32.4	30.9	**29.4**	40.7	35	**30.5**	33	32.5	**29.8**	36.2	34.9	**30.2**	34.6	38.6	**29.7**	37.9	43.2

results in the g.w.i. IPP RMS errors being worse than the corresponding n.w.i. IPP RMS errors in some cases in Tables V–VII. However, as the observation time increases, the MIMM estimator can gradually make the correct decision to find the best IMM estimator (the one with the most suitable initial drag coefficient estimate) and then, as we expect, the g.w.i. IPP results are better than the corresponding n.w.i. IPP results. Given a very short OT in a strong wind environment (e.w.i. vs. g.w.i.), the

bias in the erroneous wind information sometimes exacerbates and sometimes improves the IPP results. Generally, the e.w.i. IPP performance is between the g.w.i. and n.w.i. cases when the MIMM-selected drag coefficient estimate matches the truth.

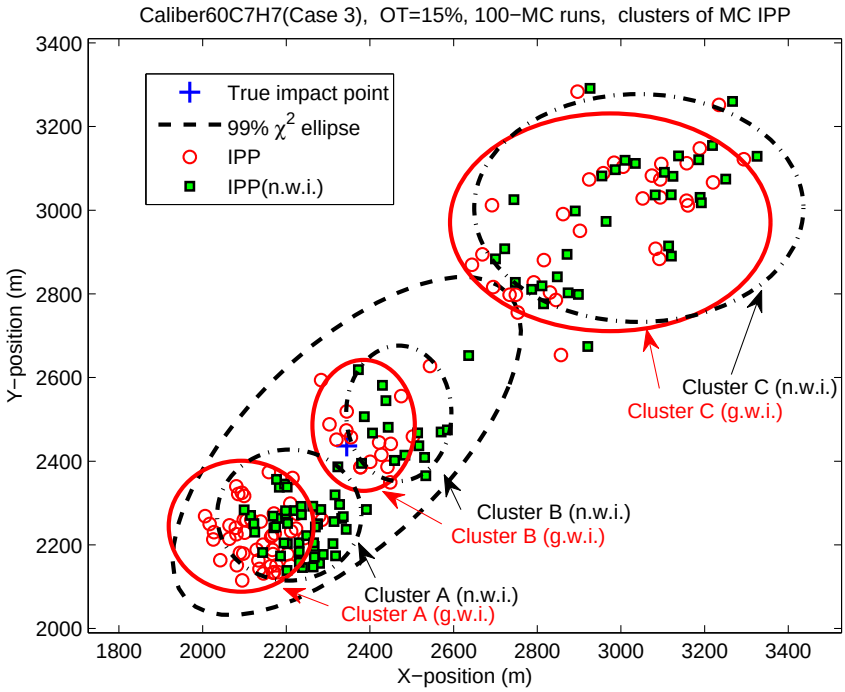

Fig. 5: The clusters of MC IPP "clould of points" caused by imperfect decision of the best IMM in MIMM estimator.

B. IPP Uncertainty Ellipse

With various OTs and sensor accuracies, the IPP uncertainty ellipses using (22), centered at the true impact point, with the corresponding *MC IPP "cloud of points"* (for both g.w.i. and n.w.i.) for various trajectories in the presence of wind are shown in Figs. 6–8.

From Fig. 6, it can be seen that as the OT increases, more IPP points fall in the corresponding uncertainty ellipses and the sizes of the uncertainly ellipses gradually shrink. The total observation time is crucial for the evaluation: given the OT is large enough (50%), most of the MC IPP points fall within the uncertainty ellipses with acceptable IPP RMS errors. The outliers are due to the forced early decision when the OT is small.

From Fig. 7, it can be seen that as the sensor accuracy worsens, the corresponding IPP uncertainty ellipses become wider because of the poor angle accuracy or become longer because of the poor range accuracy, and fewer MC IPP points fall into them. Particularly, the larger sensor errors in angles (which cause more uncertainty along the minor axis of the uncertainty ellipse in the case considered) result in the MC IPP points being more scattered along the minor axis of the corresponding IPP uncertainty ellipse; the larger sensor errors in range (which cause more uncertainty along the major axis of the uncertainty

ellipse in the case considered) result in the MC IPP points being more scattered along the major axis of the corresponding IPP uncertainty ellipse. Overall, the sensor errors along the projectile travel direction have more impact on the IPP performance.

From Fig. 8, comparing the n.w.i. IPP clouds with *smaller wind* ("C5"/"C5H5"/"C5T5") to those n.w.i. IPP clouds with *stronger wind* ("C10"/"C7H7"/"C7T7"), respectively, it is obvious that the stronger the wind is, the more significant the deviations of the n.w.i. IPP clouds are. When both the cross wind and the range wind were present, the wind-induced drift of the n.w.i. IPP clouds is compounded: without accounting for the cross wind, the n.w.i. IPP cloud deviates to one side (the right side in the cases discussed) of the major axis of the uncertainty ellipses (obtained by properly accounting for the wind effect in the dynamic model) while the lack of accounting for the range wind causes the n.w.i. IPP cloud to be "pushed backward/forward" causing range under-/over- prediction.

C. Consistency Evaluation

The consistency of the MIMM estimator is very important in the IPP application. It is always desired that the predicted impact point falls into the uncertainty ellipse centered at the true impact point (or the equivalent converse). This can be achieved by increasing the process noise intensities, which results in an ellipse with its major- and minor- axes large enough to include the predicted impact point. However, this solution is undesirable. A consistency test will help to find the process noise setting that gives the uncertainty ellipse compatible with the actual errors [1].

The consistency of the MIMM estimator is examined using both the normalized estimation error squared (NEES), which is preferable for Monte Carlo runs when the truth is available (off-line simulations), and the normalized innovation squared (NIS). The latter is the only one that can be used in real time testing [1].

Fig. 9 shows, for the best IMM estimator selected from the MIMM estimator with OT=50% and various sensor accuracies, the NEES consistency in position and velocity and the NIS. Note that the NIS is evaluated for TM before the *estimated* BoP and for BM afterward [15]. It can be seen that as the sensor errors increase, the IMM estimator selected becomes less consistent. In particular, the larger the sensor's range error (which causes more uncertainty along the travel direction of the projectiles in present cases), the more significant is the inconsistency.

VI. Summary and Conclusions

The MIMM estimator developed in [15] has been extended to account for the wind effect. The IPP performance for various total observation times and sensor accuracies have been investigated in detail. The wind effect can be fully compensated if the wind information is available; it also can be mitigated by increasing the total observation time if no wind information is provided. The total observation time is key for IPP performance: for example, given the observations all the way up to the

apogee one can always expect a very good IPP performance, but this is clearly not desirable if countermeasures are to be taken against the projectile. The N-point initialization, designed for initializing the key thrust component as well as the kinematic components, is considered a good method to quicken the correct mode convergence in each IMM estimator and alleviate the estimation ambiguity between the drag coefficient and the thrust components. In the cases studied here, an OT of 20% or more and sensor accuracies under $10\,\mathrm{m}$ in range and $5\,\mathrm{mrad}$ in angles are required to overcome the marginal observability (ambiguity) of the drag and thrust and then achieve an acceptable IPP performance, with the IPP RMS error no more than 10% of the projectile range. The sensor errors that cause more uncertainty along the travel direction of the projectiles have more impact on the IPP performance. In the presence of wind, the short observation time and the limited sensor accuracy are more critical since they could cause confusion in selecting the "correct" best IMM estimator (which should be the one with the most suitable initial drag coefficient estimate, closest to truth) from the MIMM estimator, and then lead to a degraded IPP performance.

APPENDIX A
CUBIC SPLINE INTERPOLATION

As shown in Fig. 10, the cubic spline curve of the Mach number-dependent drag coefficient multiplier is obtained by interpolating the selected representative points shown in Table VIII.

TABLE VIII: Selected representative points for cubic spline interpolation

Speed (m/s)	1	50	100	150	190	230	280	285	295	310	350
Normalized drag coefficient	1	1.01	1.015	1.02	1.03	1.035	1.1	1.2	1.3	1.4	1.59
Speed (m/s)	400	440	500	550	590	650	750	800	850	1000	1000+
Normalized drag coefficient	1.69	1.71	1.68	1.55	1.4	1.35	1.33	1.32	1.31	1.3	1.3

REFERENCES

[1] Y. Bar-Shalom, X. R. Li and T. Kirubarajan, *Estimation with Applications to Tracking and Navigation: Algorithms and Software for Information Extraction*, Wiley, 2001.

[2] Y. Bar-Shalom, P. K. Willett and X. Tian, *Tracking and Data Fusion*, YBS Publishing, Storrs, CT, 2011.

[3] D. E. Carlucci and S. S. Jacobson, *Ballistics: Theory and Design of Guns and Ammunition*, CRC Press, 2007.

[4] A. Farina, L. Timmoneri and D. Vigilante, "Classification and Launch-Impact Point prediction of Ballistic Target via Multiple Model Maximum Likelihood Estimator (MM-MLE)", *Proc. IEEE Radar Conference '06*, Verona NY, 2006.

[5] X. R. Li and V. P. Jilkov, "Survey of Maneuvering Target Tracking. Part II: Motion Models of Ballistic and Space Targets", *IEEE Trans. Aerosp. Electronic Systems*, 46(1): 96-119, Feb. 2010.

[6] R. L. McCoy, *Modern Exterior Ballistics: The Launch and Flight Dynamics of Symmetric Projectiles*, Schiffer Publishing Limited, 1999.

[7] R. K. Mehra, "A Comparison of Several Nonlinear Filters for Reentry Vehicle Tracking", *IEEE Trans. Automatic Control*, AC-16(4): 307-319, Aug. 1971.

[8] T. Nishimura, "On the a Priori Information in Sequential Estimation Problems", *IEEE Trans. Automatic Control*, Vol.11(2): 197-204, Apr. 1966.

[9] R. W. Osborne, III, Y. Bar-Shalom and T. Kirubarajan, "Radar Measurement Noise Variance Estimation with Several Targets of Opportunity", *IEEE Trans. Aerosp. Electronic Systems*, 44(3): 985-995, July 2008.

[10] R. W. Osborne, III and Y. Bar-Shalom, "Statistical Efficiency of Composite Measurements from LoS Observation", *Proc. SPIE Conf. Signal Processing, Sensor Fusion and Target Recognition*, #8050-07, Orlando FL, April 2011.

[11] W. H. Press, B. P. Flannery, S. A. Teukolsky and W. T. Vetterling, *Numerical Recipes in FORTRAN: The Art of Scientific Computing, 2nd ed*, Cambridge University Press, 1992.

[12] V. Ravindra, Y. Bar-Shalom and P. K. Willett, "Projectile Identification and Impact Point Prediction", *IEEE Trans. Aerosp. Electronic Systems*, 46(4): 2004-2021, Oct. 2010.

[13] F. Reali, G. Palmerini, A. Farina A. Graziano, S. Giompapa and B. Parisi, "Initialization of Ballistic Target Tracking Filters with Detection Probability Lower than Unity", *IEEE Aerospace Conference '10*, Big Sky, Montana, USA, March 6-13, 2010.

[14] T. Yuan, Y. Bar-Shalom, P. K. Willett and D. Hardiman, "Impact Point Prediction for Short Range Thrusting Projectiles", *Proc. SPIE Conf. Signal and Data Processing of Small Targets*, #7698-55, Orlando FL, April 2010.

[15] T. Yuan, Y. Bar-Shalom, P. K. Willett, E. Mozeson, S. Pollak and D. Hardiman, "A Multiple IMM Estimation Approach with Unbiased Mixing for Thrusting Projectiles", *IEEE Trans. Aerosp. Electronic Systems*, 48(4):3250–3267, Oct. 2012.

[16] U.S. Army, "GTRAJ, General Trajectory Program, US Army".

[17] http://www.braeunig.us/space/cd.htm

[18] http://en.wikipedia.org/wiki/External_ballistics

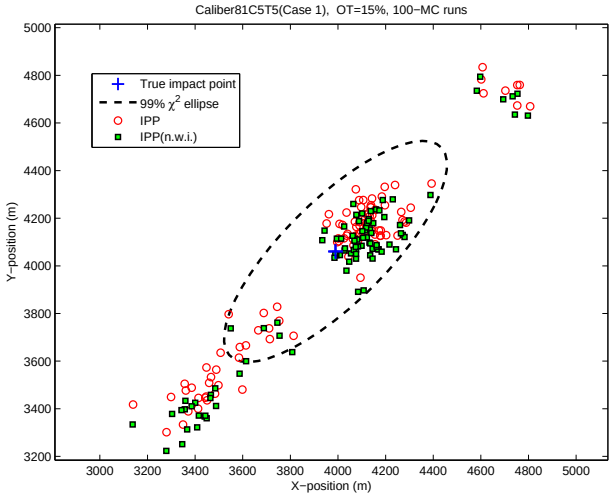

(a) OT=15%

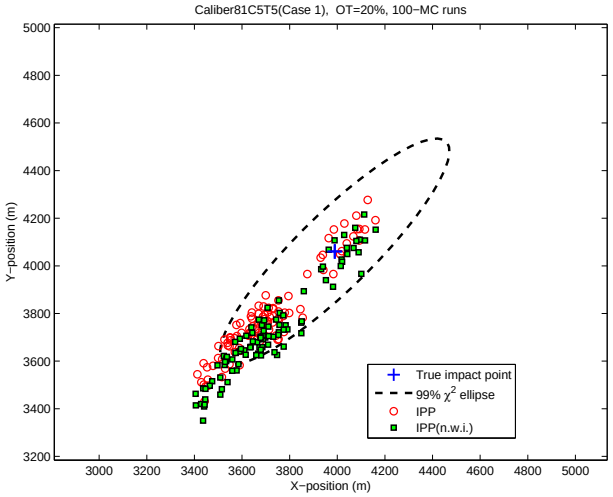

(b) OT=20%

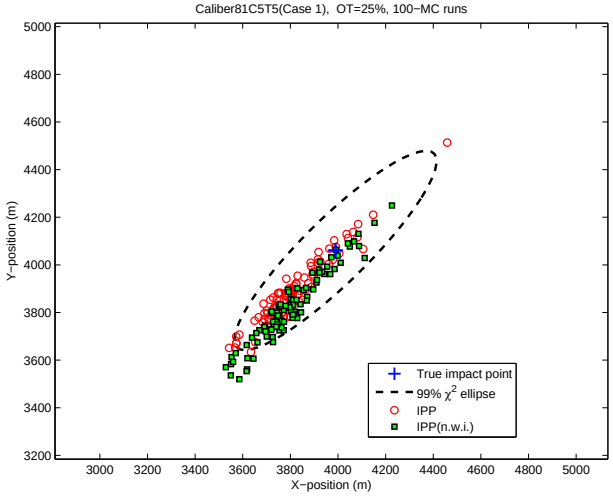

(c) OT=25%

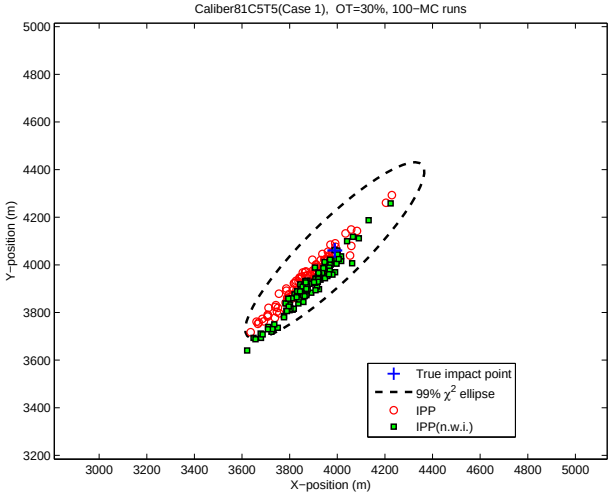

(d) OT=30%

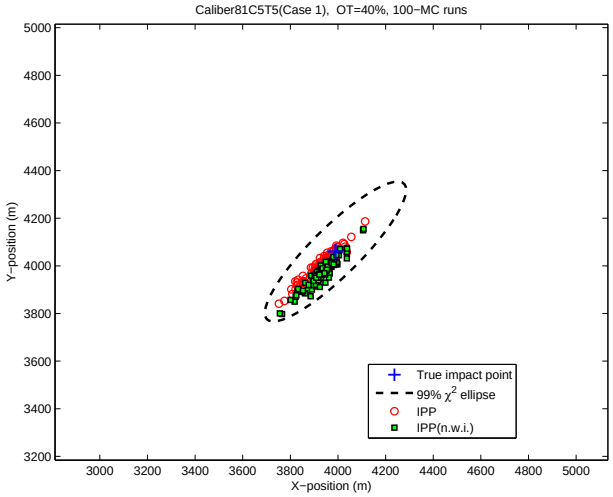

(e) OT=40%

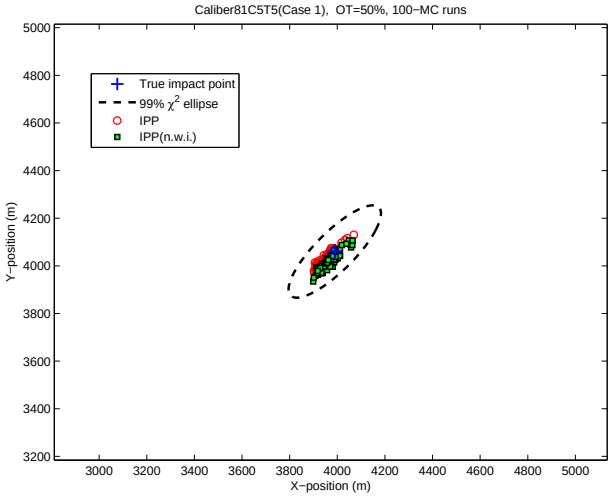

(f) OT=50%

Fig. 6: IPP uncertainty ellipse and MC IPP cloud for *various OTs*, trajectory 81C5T5, $Case$ 1, 100 MC runs

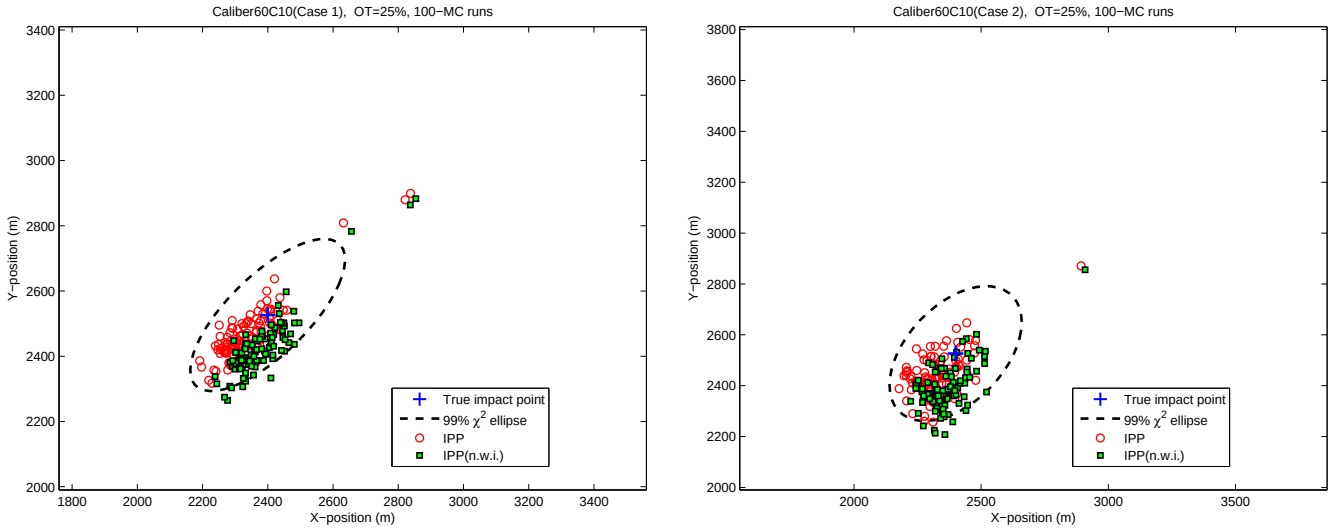

(a) $Case$-1 (good accuracy)

(b) $Case$-2 (poor angle accuracies)

(c) $Case$-3 (poor range accuracy)

(d) $Case$-4 (best accuracy)

Fig. 7: IPP uncertainty ellipse and MC IPP cloud for *various sensor accuracies*, trajectory 60C10, OT=25%, 100 MC runs

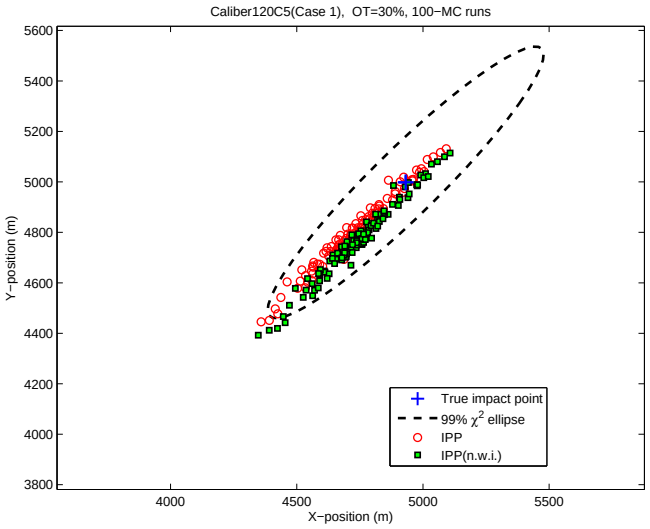

(a) Trajectory 120C5

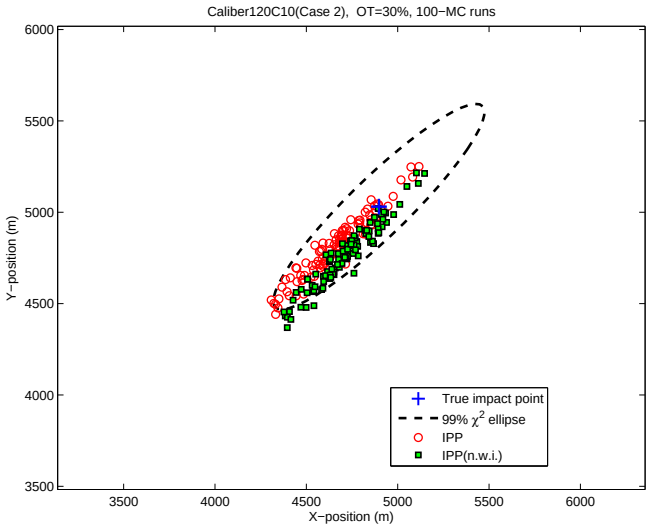

(b) Trajectory 120C10

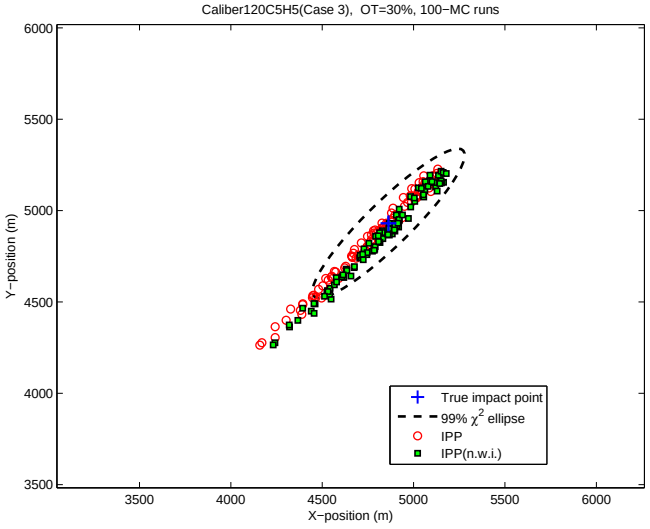

(c) Trajectory 120C5H5

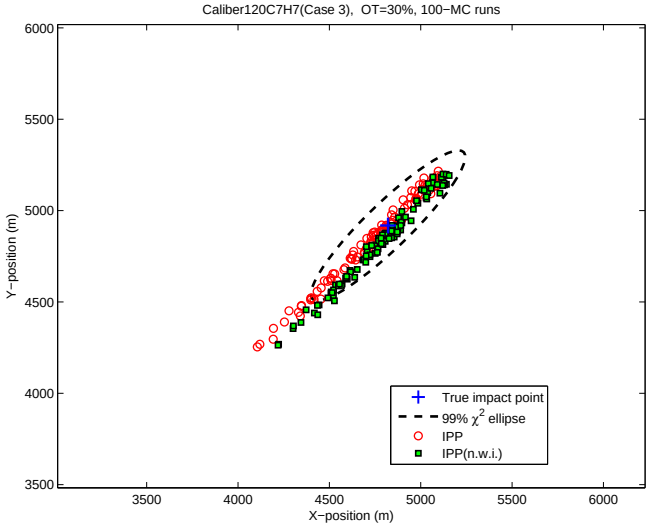

(d) Trajectory 120C7H7

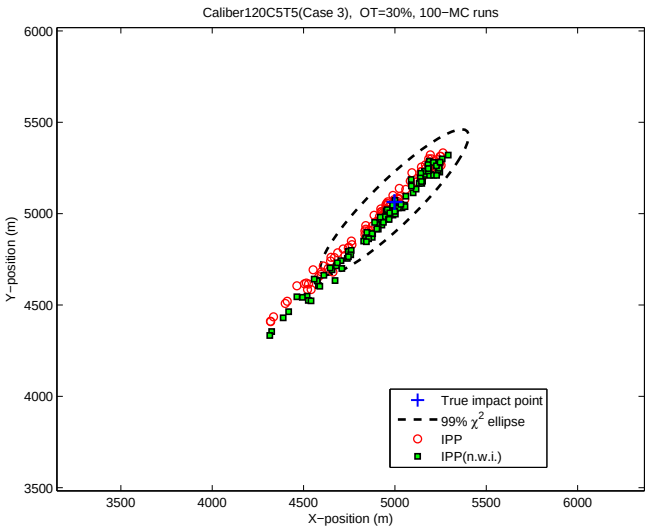

(e) Trajectory 120C5T5

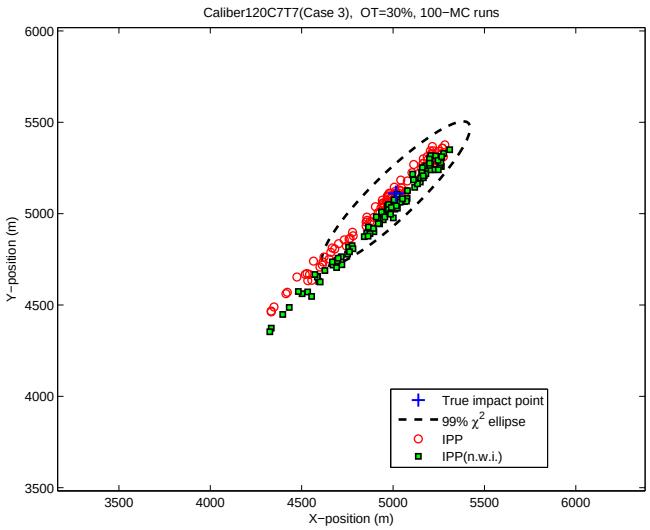

(f) Trajectory 120C7T7

Fig. 8: The IPP uncertainty ellipse and MC IPP cloud for various 120mm trajectories, OT=30% 100 MC runs

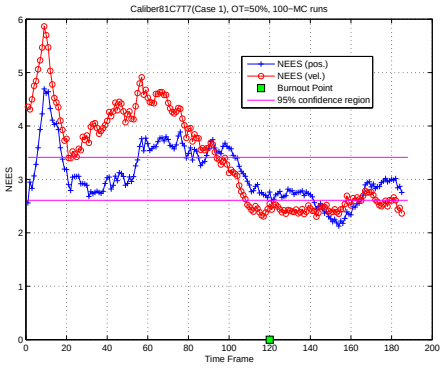

(a) NEES (pos. and vel.), g.w.i., $Case$ 1

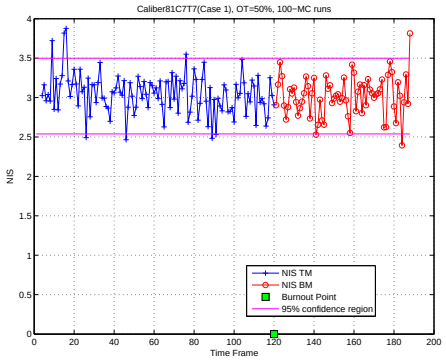

(b) NIS, g.w.i., $Case$ 1

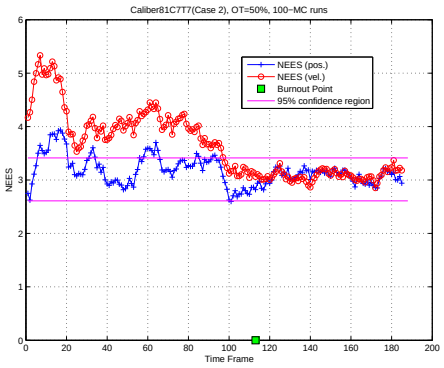

(c) NEES (pos. and vel.), g.w.i., $Case$ 2

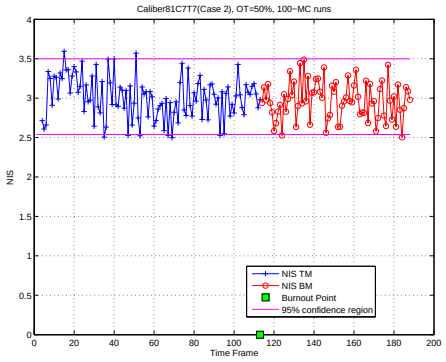

(d) NIS, g.w.i., $Case$ 2

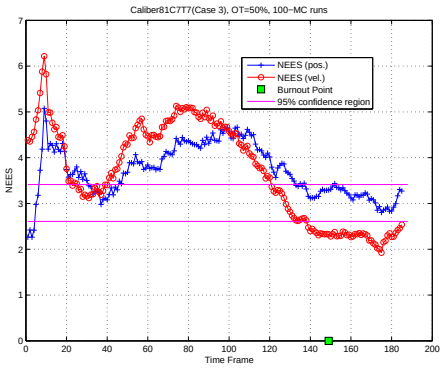

(e) NEES (pos. and vel.), g.w.i., $Case$ 3

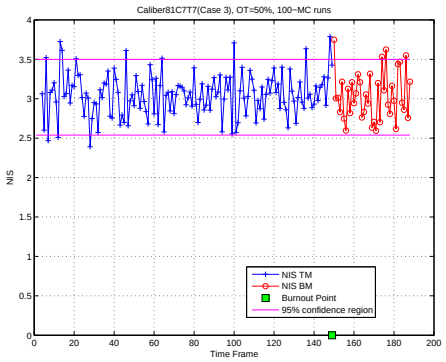

(f) NIS, g.w.i., $Case$ 3

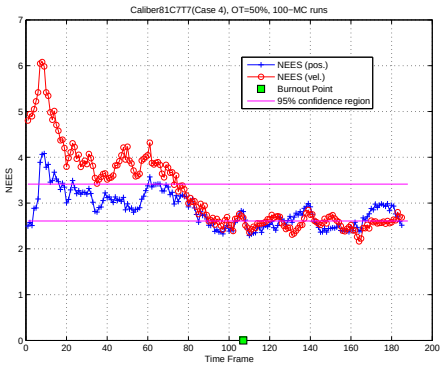

(g) NEES (pos. and vel.), g.w.i., $Case$ 4

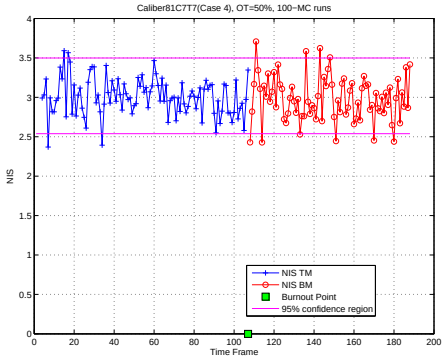

(h) NIS, g.w.i., $Case$ 4

Fig. 9: Consistency test (NEES in pos. and vel. and NIS), trajectory 81C7T7, OT=50%, 100-MC run

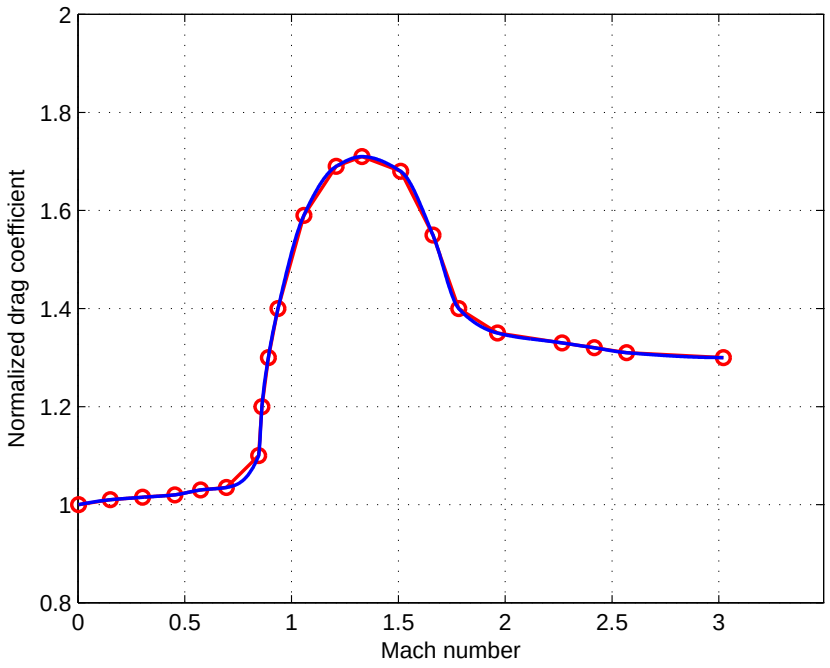

Fig. 10: The cubic spline approximation (for a “sharp nose” projectile [17]).